Supplementary Information

Graphene-enabled laser lift-off for ultrathin displays

Sumin Kang[1], Jaehyeock Chang[2], Jaeseung Lim[3,4], Dong Jun Kim[5], Taek-Soo Kim[5], Kyung Cheol Choi[2], Jae Hak Lee[3], Seungman Kim[3,4,6*]

[1] Department of Mechanical and Automotive Engineering, Seoul National University of Science and Technology, Seoul 01811, Republic of Korea

[2] School of Electrical Engineering, Korea Advanced Institute of Science and Technology, Daejeon 34141, Republic of Korea

[3] Semiconductor Manufacturing Research Center, Korea Institute of Machinery and Materials, Daejeon 34103, Republic of Korea

[4] Department of Robot·Manufacturing Systems, University of Science and Technology, Daejeon 34113, Republic of Korea

[5] Department of Mechanical Engineering, Korea Advanced Institute of Science and Technology, Daejeon 34141, Republic of Korea

[6] Wm Micheal Barens'64 Department of Industrial and Systems Engineering, Texas A&M University, College Station, TX 77843, USA

[*]Author for correspondence: kimsm@kimm.re.kr

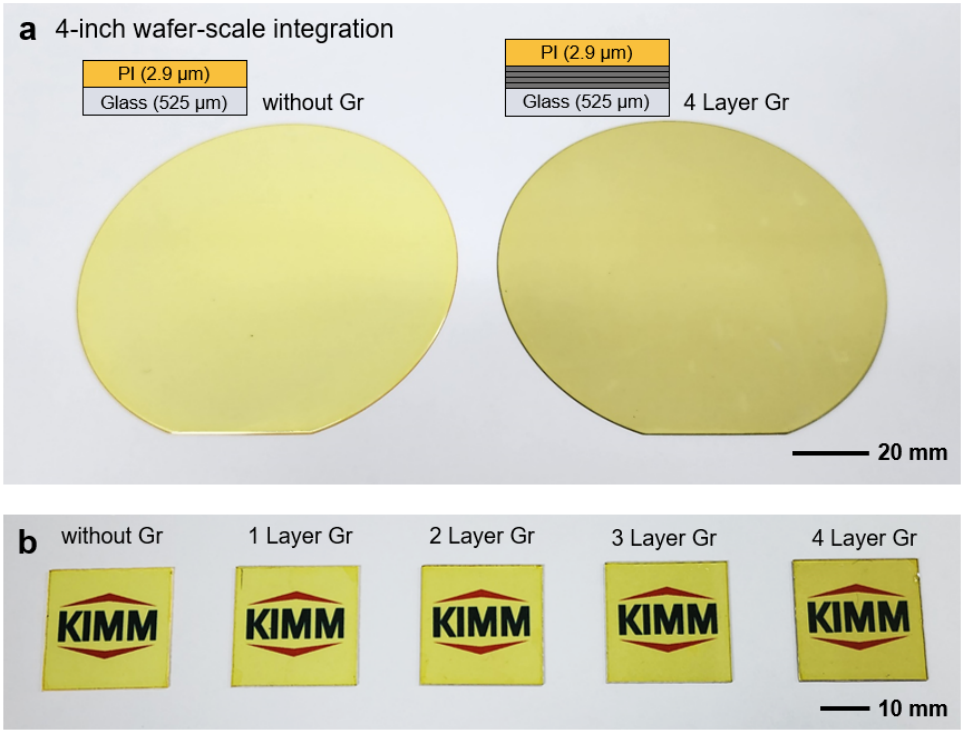

Supplementary Fig. 1 | Prepared glass carrier–graphene–PI film structured specimens. **a**, 4-inch wafer-scale specimens without graphene and with the integration of 4-layered graphene. **b**, 25 x 25 mm^2 square specimens for various numbers of integrated layers.

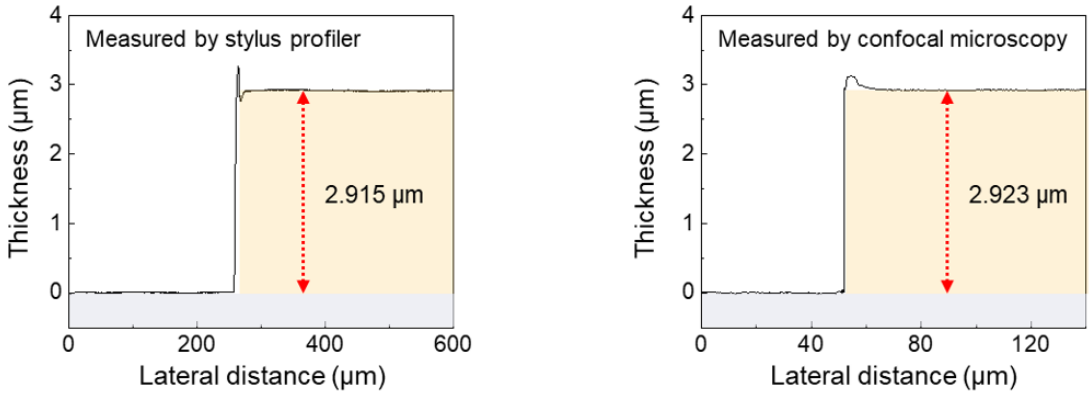

Supplementary Fig. 2 | The thickness of the fabricated ultrathin PI film measured by stylus profiler and confocal microscopy.

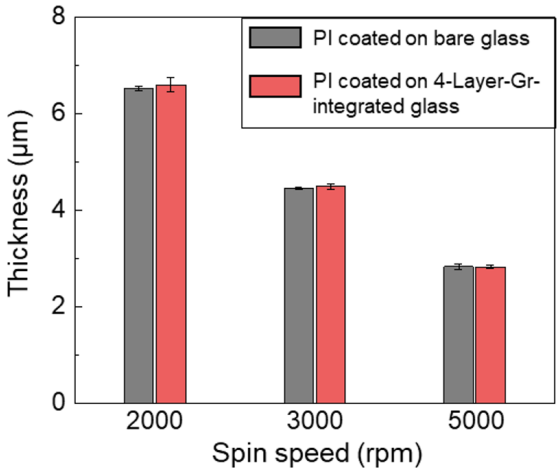

Supplementary Fig. 3 | The measured thickness of the PI films spin-coated on bare glass carrier and 4-layer-graphene-integrated glass carrier.

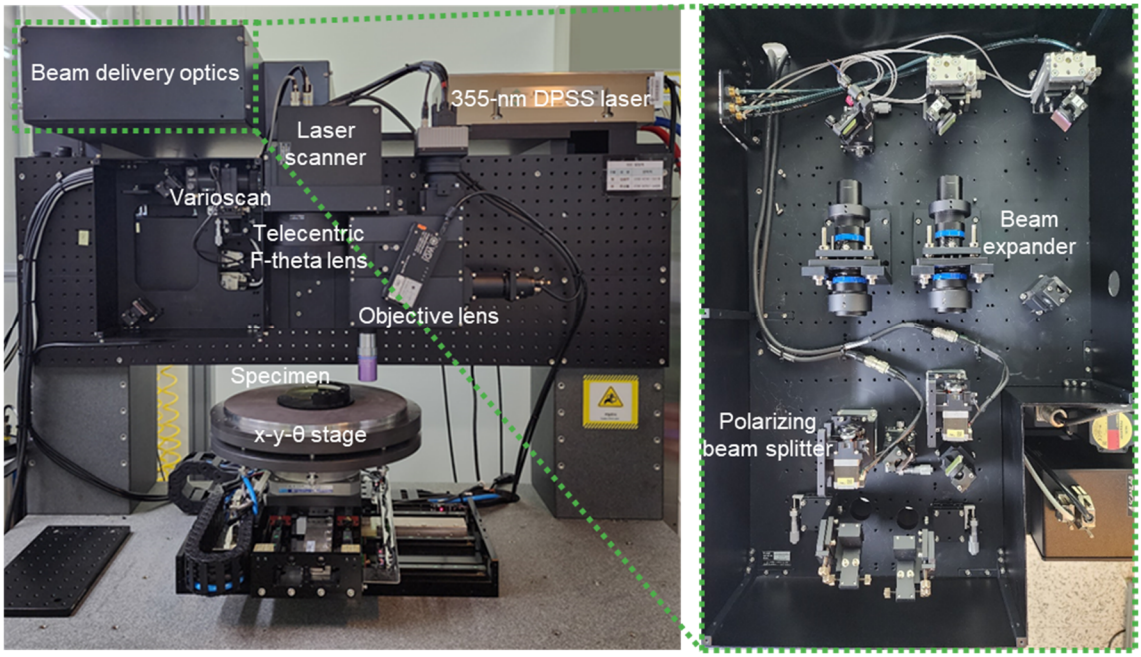

Supplementary Fig. 4 | 355 nm DPSS laser and optical system.

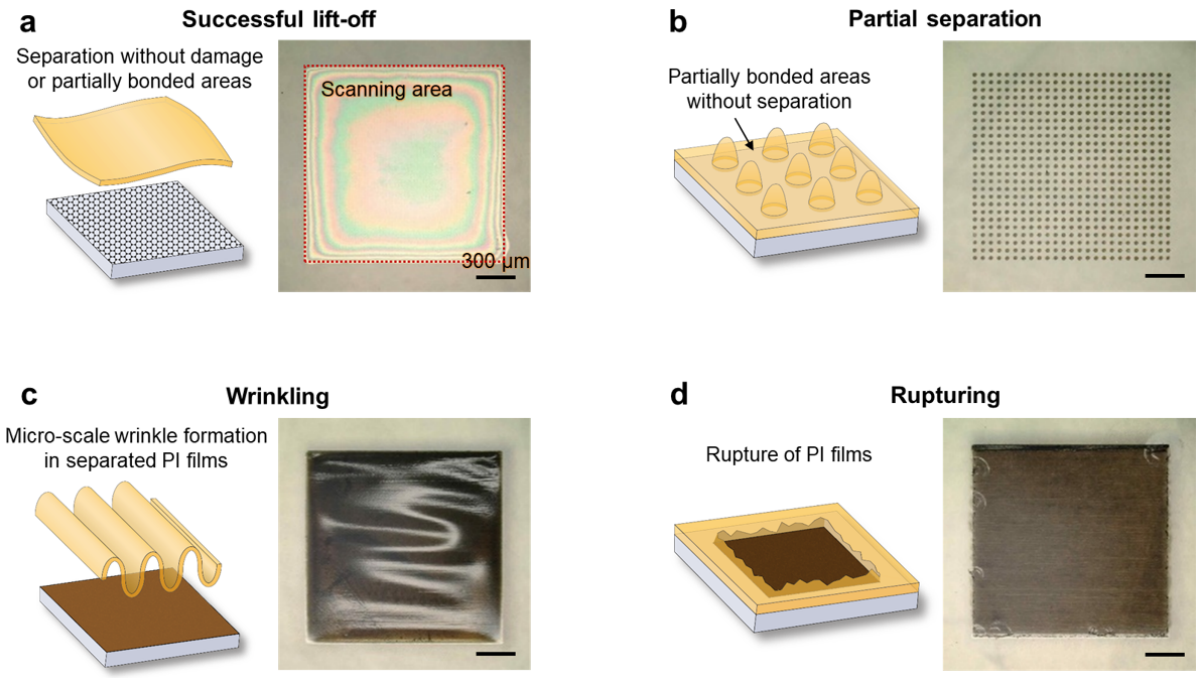

Supplementary Fig. 5 | Classification of the lift-off results and representative OM images. **a**, Successful lift-off is defined as the separation of the PI films without micro-scale wrinkles, ruptures, and partially bonded areas. **b**, Partial separation is defined as the presence of remaining bonded areas without separation. **c**, Wrinkling is defined as the presence of micro-scale wrinkles in the separated PI films. **d**, Rupturing is defined as the tearing of separated PI films due to mechanical deformation exceeding their fracture toughness.

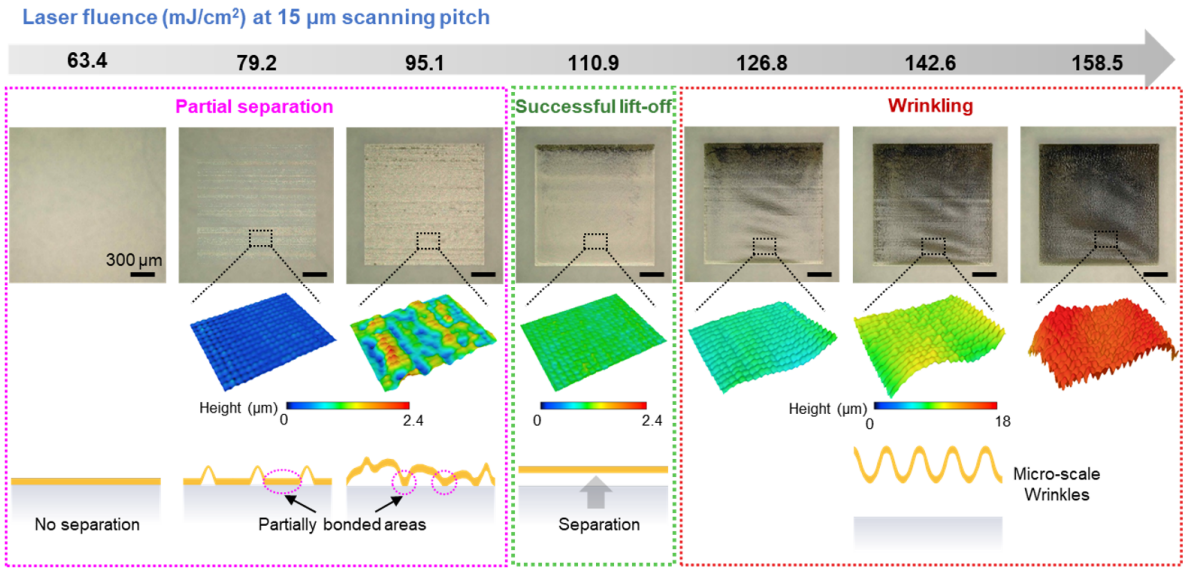

Supplementary Fig. 6 | Analysis of lift-off OM images obtained by the conventional LLO method. Confocal microscopy images (scale factor: 10) and corresponding schematics illustrate the lift-off behaviors of the PI film in detail under various laser fluence conditions.

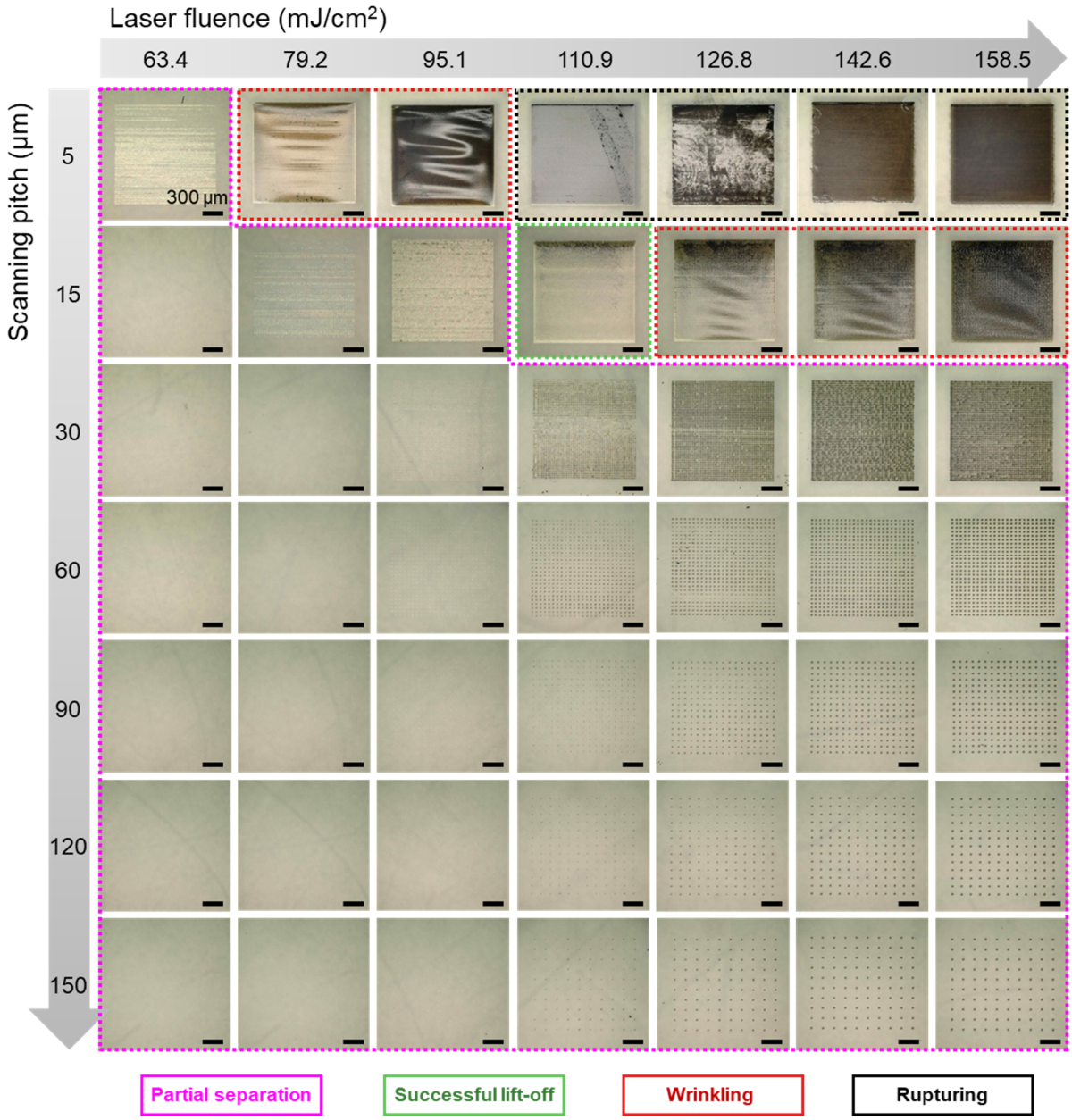

Supplementary Fig. 7 | OM images of conventional-LLO-processed PI films with respect to the laser fluence and scanning pitch.

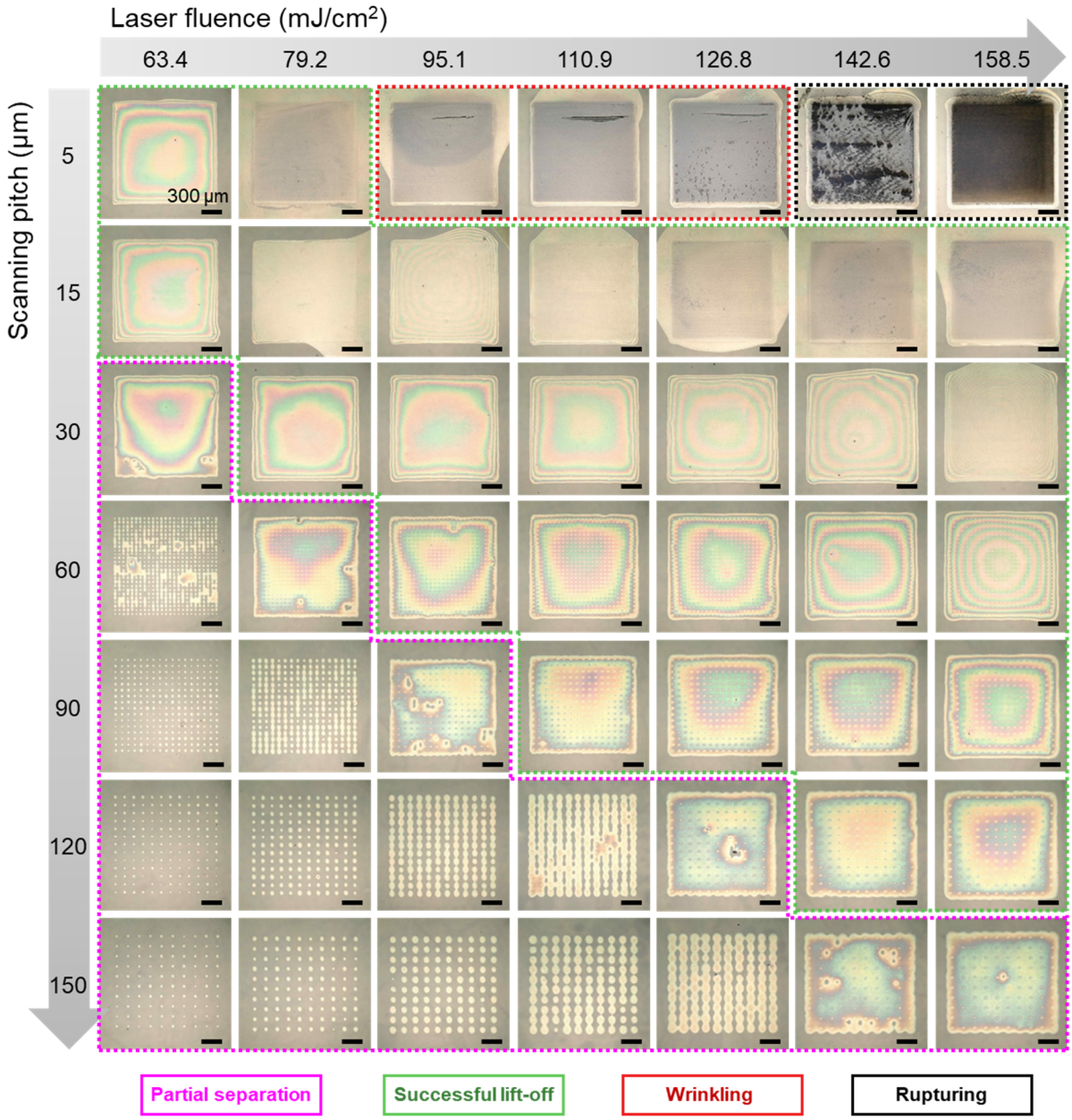

Supplementary Fig. 8 | OM images of GLLO-processed PI films with respect to the laser fluence and scanning pitch.

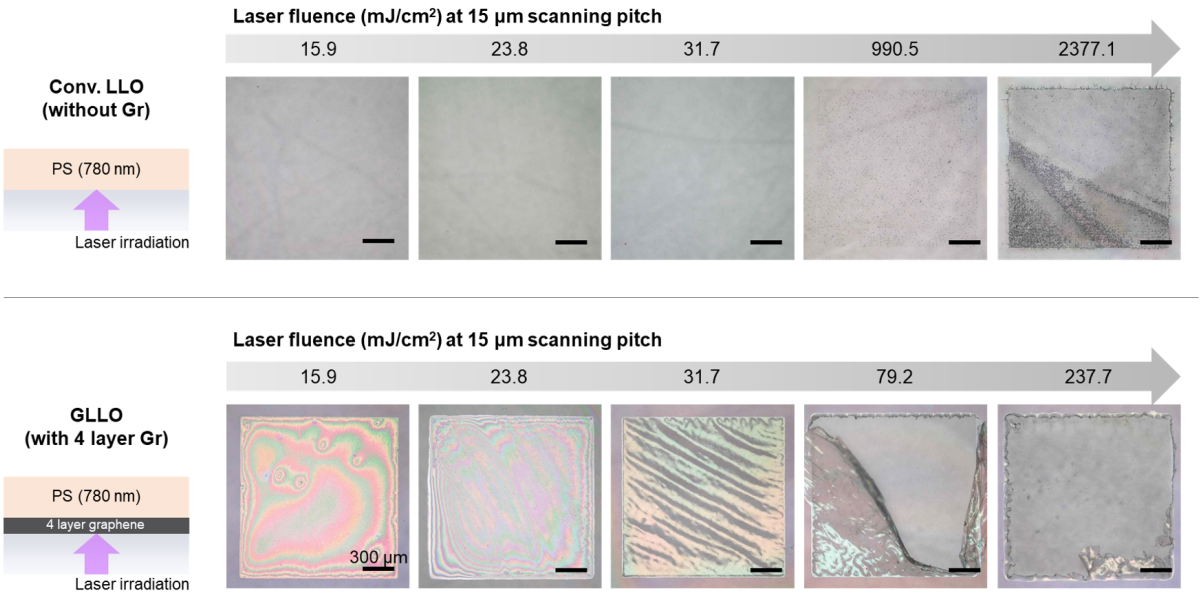

Supplementary Fig. 9 | Application of the GLLO method to a 780-nm-thick polystyrene (PS) thin film. For the conventional LLO process, the low thermal stability of the PS film resulted in no observable differences at low fluence conditions and the formation of an ablation trail without separation at high fluence conditions. In contrast, the GLLO process enabled the lift-off of the PS film under low laser fluence conditions. The separation mechanism of the PS film can be attributed to a photomechanical effect, which indicates that separation occurred at temperatures slightly above the glass transition temperature (T_g) due to the coefficient of thermal expansion (CTE) mismatch[S1]. It is anticipated that the graphene layer enlarged the CTE mismatch effect, including the enhancement of interfacial UV absorption, lateral heat diffusion, and adhesion reduction.

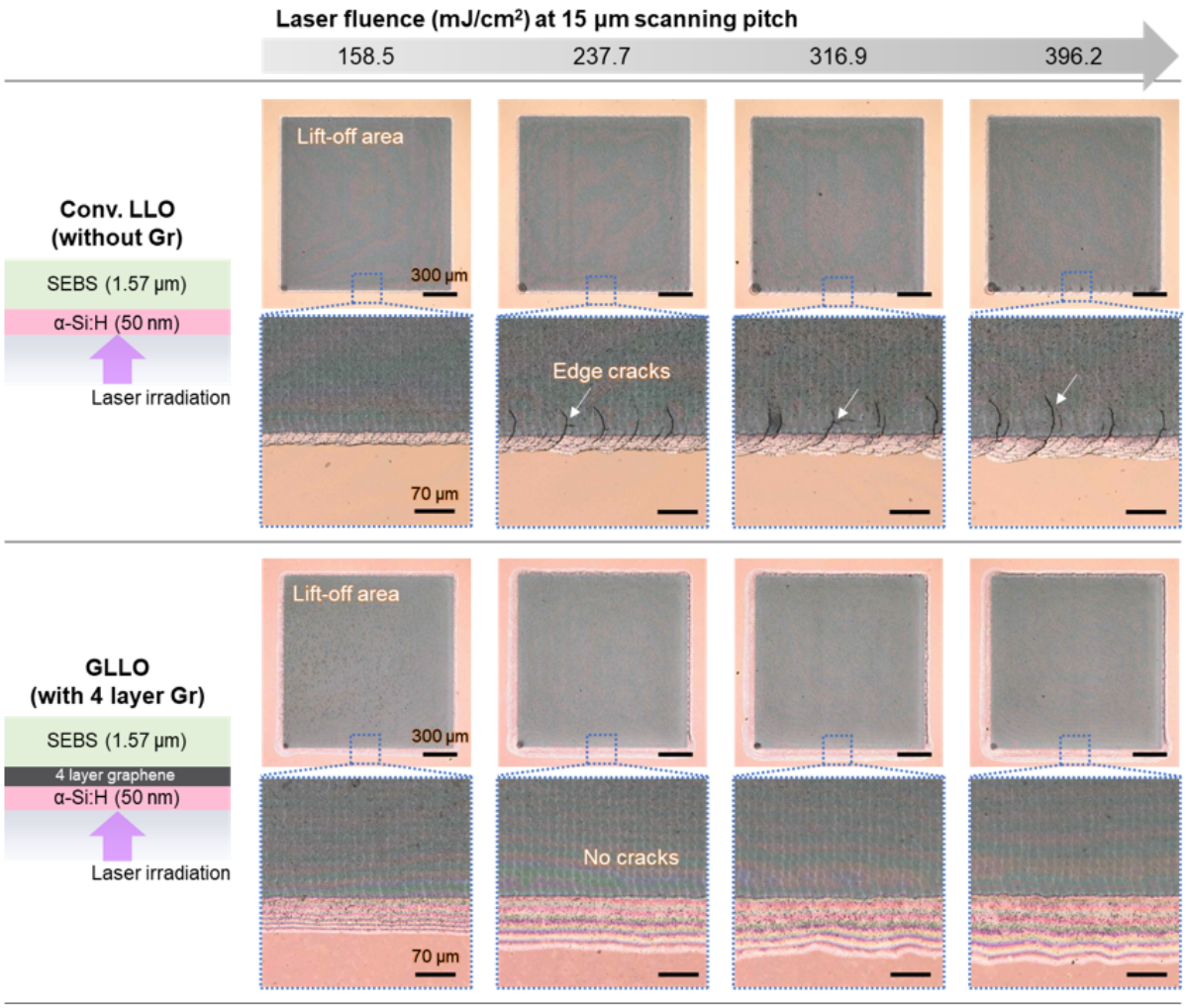

Supplementary Fig. 10 | Application of the GLLO method to a material system composed of a 50-nm-thick hydrogenated amorphous silicon (α-Si:H) layer and a 1.57-μm-thick polystyrene-*b*-poly(ethylene-*co*-butylene)-*b*-polystyrene (SEBS) elastomer film. The α-Si:H was utilized as a sacrificial layer for the laser ablation process, and the graphene layer was inserted between the α-Si:H layer and SEBS film. The results indicate that edge cracks were observed under high laser fluence conditions in the conventional LLO processes, although the SEBS film exhibits superior elongation of approximately 800 %[S2]. In contrast, the graphene layer prevented cracking during the lift-off processes, demonstrating the effectiveness of the GLLO method in a different material system not only the PI film.

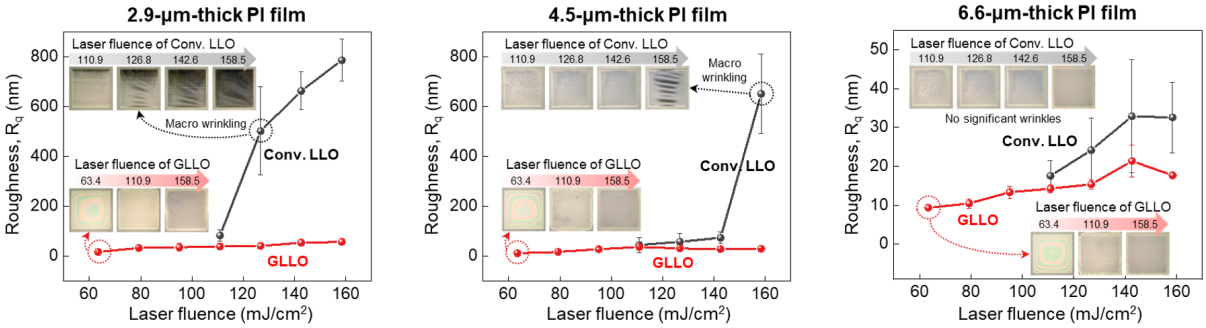

Supplementary Fig. 11 | Surface roughness of PI films with thicknesses of 2.9, 4.5, and 6.6 μm separated by conventional LLO and GLLO methods. The surface roughness was measured by confocal microscopy, and the inset shows OM images of the lift-off area under each condition. The results indicate that the differences in surface roughness between the conventional LLO and GLLO methods were mitigated due to increased bending stiffness in thicker PI films. The integrated graphene layer enabled a lower laser fluence lift-off process.

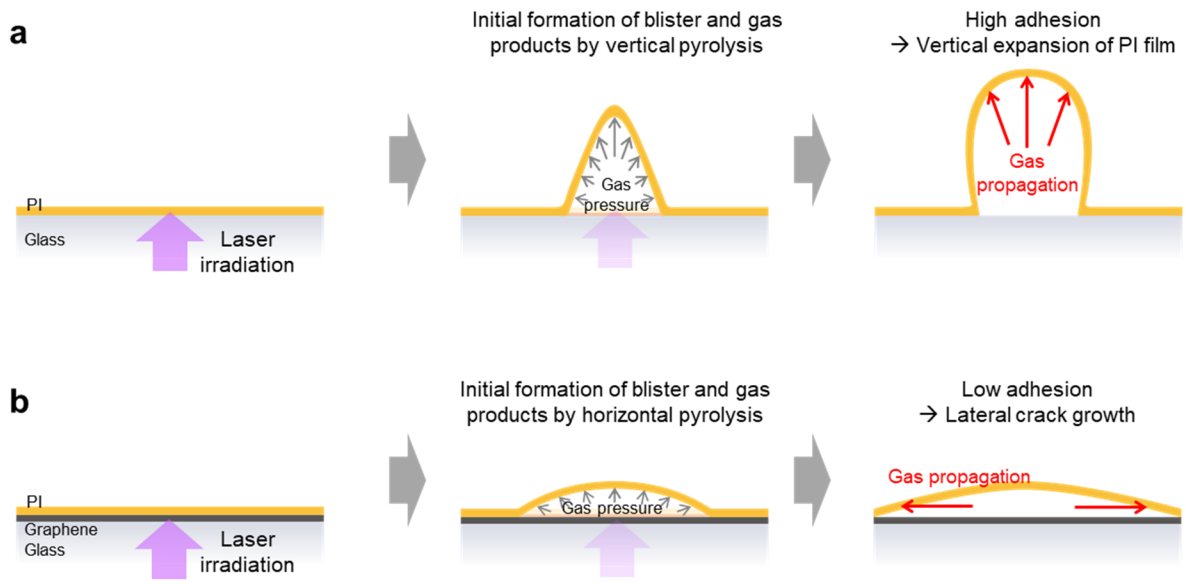

Supplementary Fig. 12 | Separation and deformation mechanisms of the PI film: **a**, conventional LLO process. **b**, GLLO process.

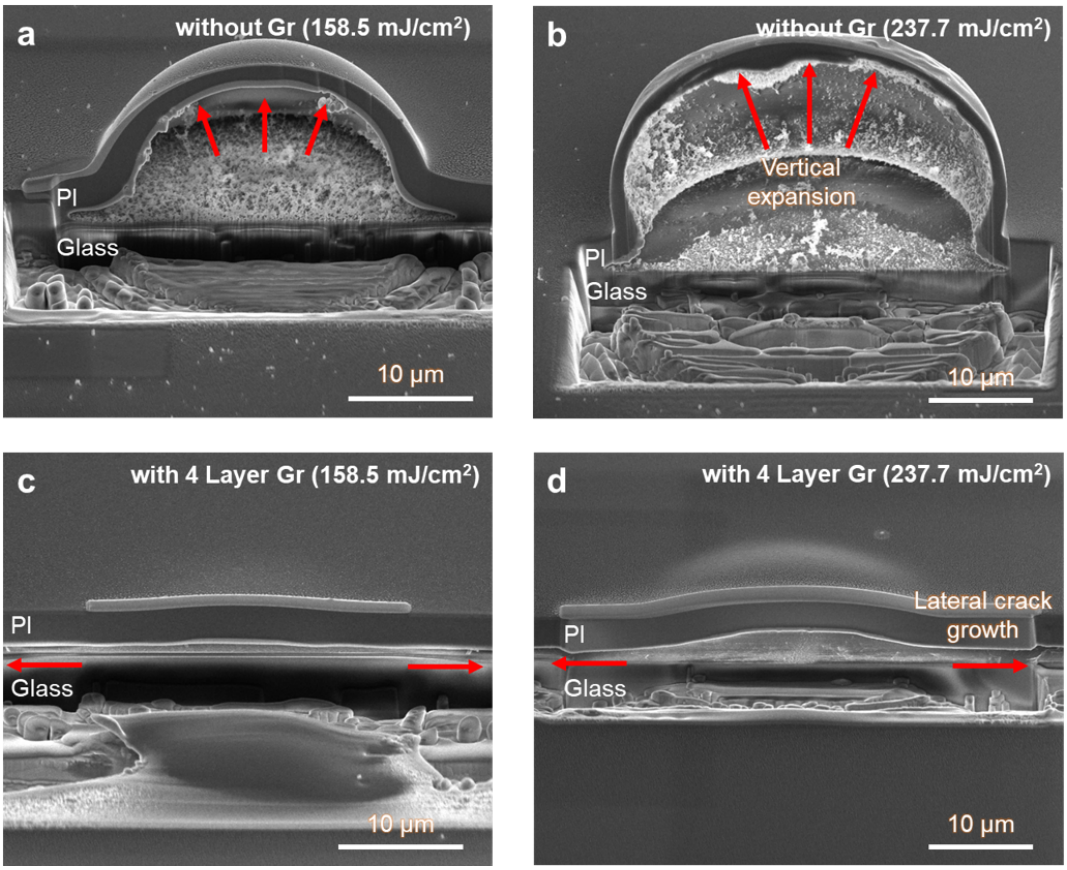

Supplementary Fig. 13 | Cross-sectional images of ultrathin PI blisters formed by laser irradiation. **a,b**, Specimens without graphene integration irradiated with a laser fluence of 158.5 and 237.7 mJ/cm^2, respectively. **c,d,** Specimens with 4-layer graphene integration irradiated with a laser fluence of 158.5 and 237.7 mJ/cm^2, respectively. The images were obtained using FEM-SEM. The FIB cuts were made along the central line of the blister, and SEM was exploited to capture the high-resolution images. A thin platinum layer was coated on the specimens to prevent deformation of the blister during the FIB milling process.

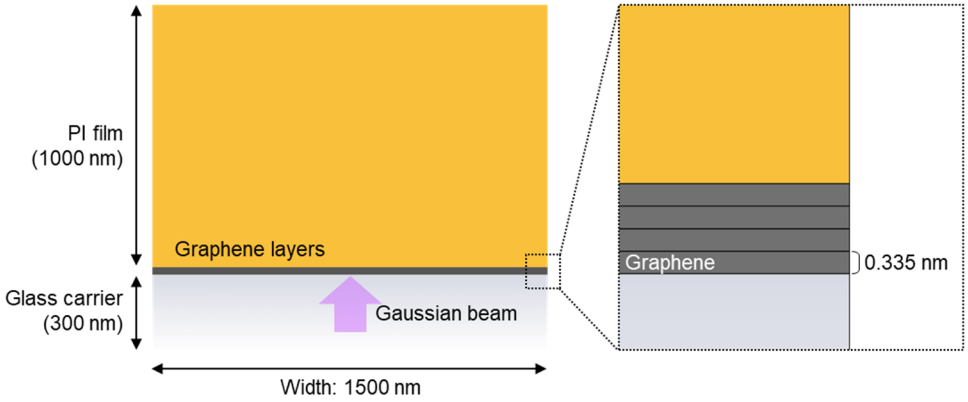

Supplementary Fig. 14 | Reduced simulation model for visualizing the relative differences in temperature profiles with respect to the number of graphene layers.

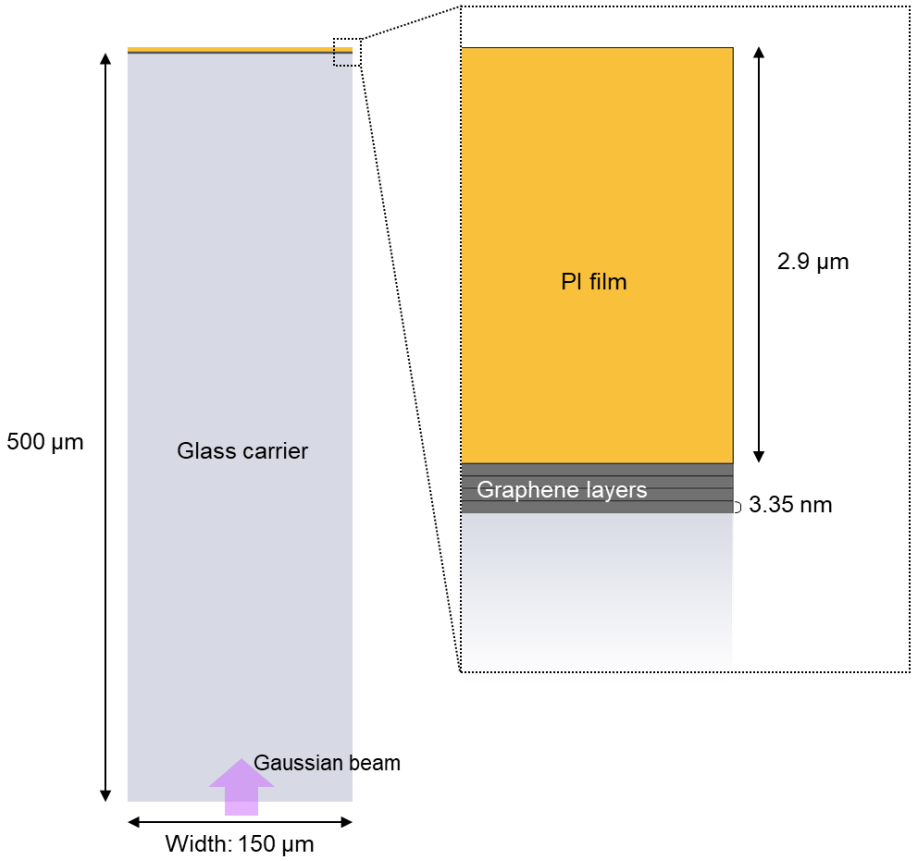

Supplementary Fig. 15 | Full-scale simulation model for accurate analysis of temperature distributions.

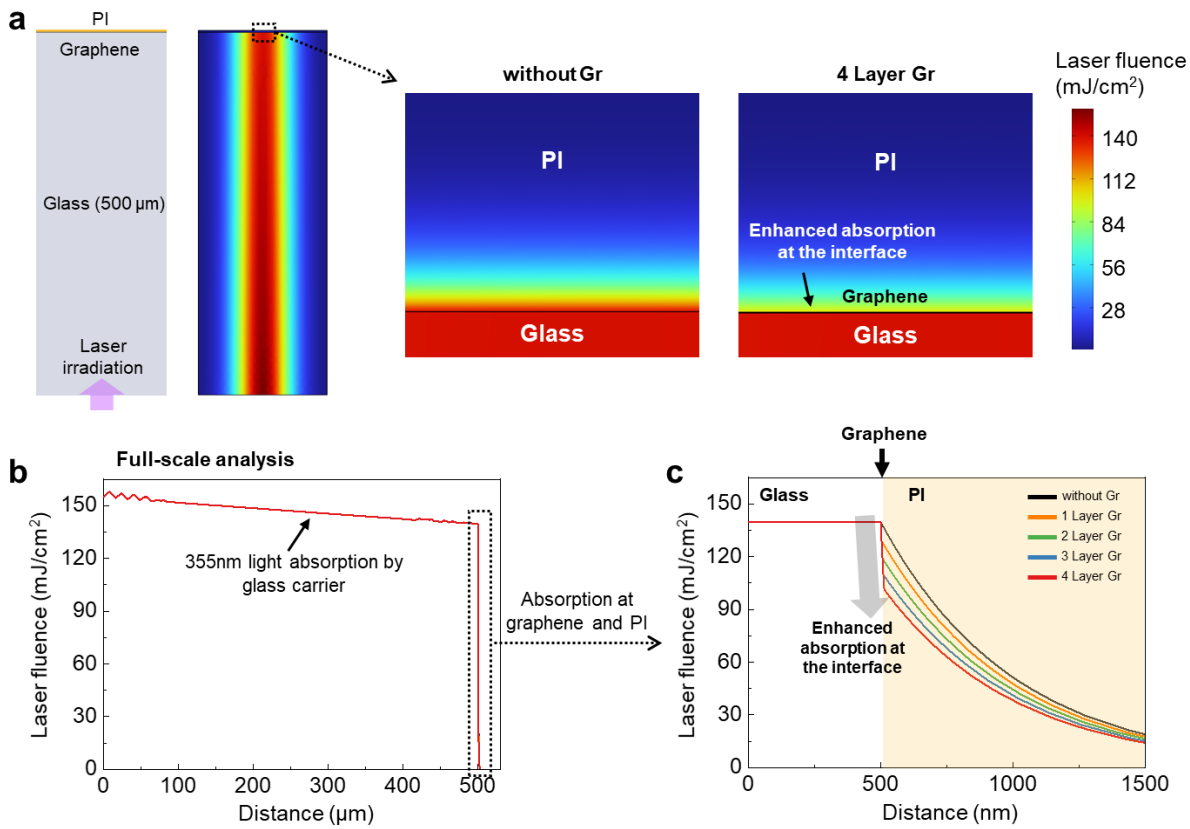

Supplementary Fig. 16 | **a**, Laser fluence profiles obtained in the FEA simulation. The graphene layer enabled the enhancement of UV light absorption at the interface. **b**, Laser fluence distribution in the vertical direction of the full-scale model. **c**, Laser fluence distribution at the graphene and PI film.

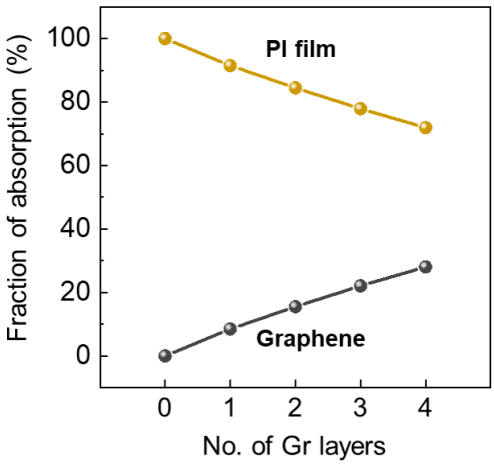

Supplementary Fig. 17 | Fraction of UV light absorption by the graphene and PI film.

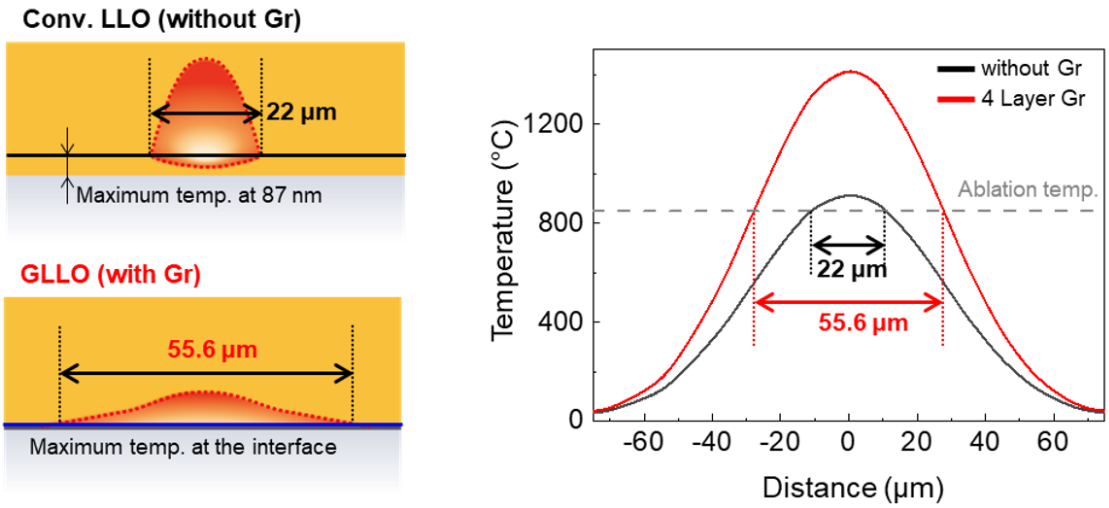

Supplementary Fig. 18 | Horizontal temperature distribution and ablation diameter at the height of maximum temperature for the conventional LLO (87 nm above the interface) and GLLO (at the interface) methods. Ablation diameters were determined by considering the threshold temperature of 850 °C for the PI films

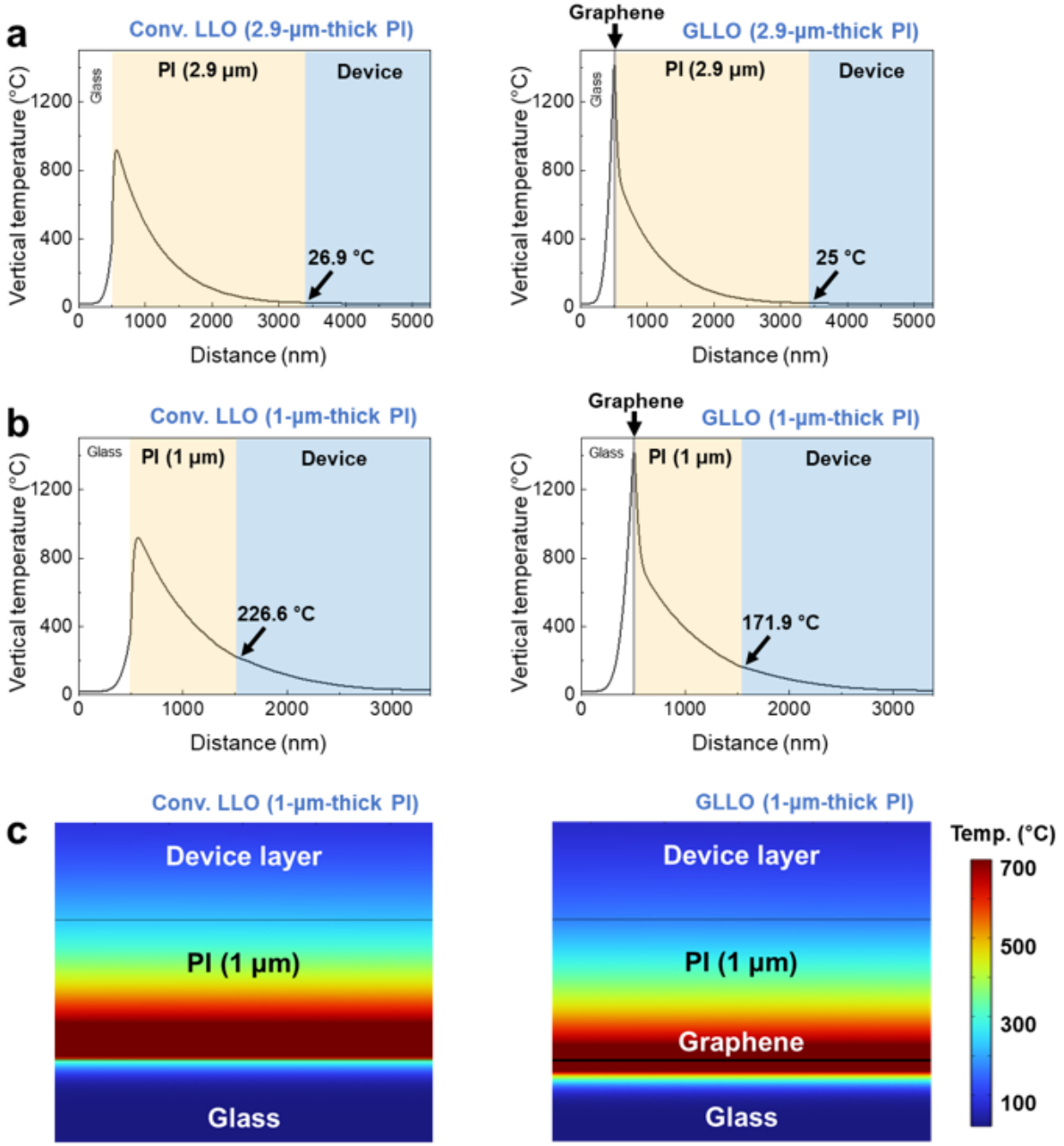

Supplementary Fig. 19 | The effect of graphene on the thermal protection of a device layer. **a**,**b**, Temperature distributions of a device layer integrated simulation model during the conventional and GLLO processes: (**a**) 2.9-μm-thick PI film, (**b**) 1-μm-thick PI film. **c**, Differences in temperature profile between the conventional and GLLO processes. The graphene layer reduced the device temperature, and the effect was more significant in thinner PI films.

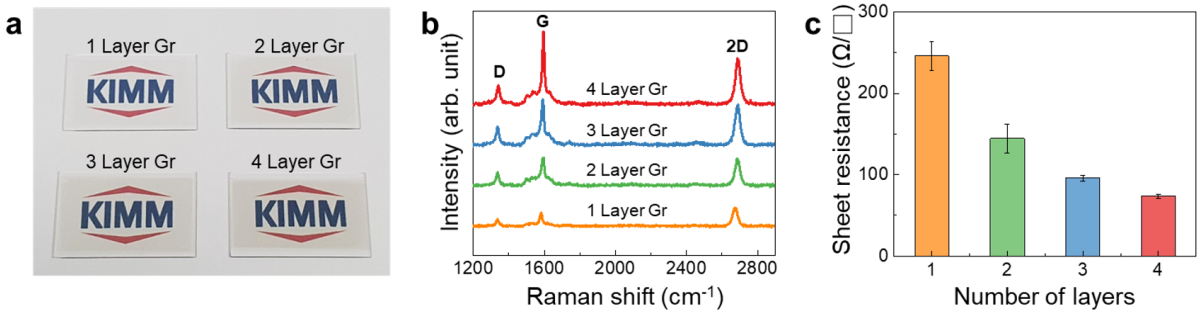

Supplementary Fig. 20 | Characterization of the transferred graphene layers. **a**, Photographs of graphene-integrated glass carriers. **b**,c Raman spectrum and sheet resistance of the gaphene layers, respectively.

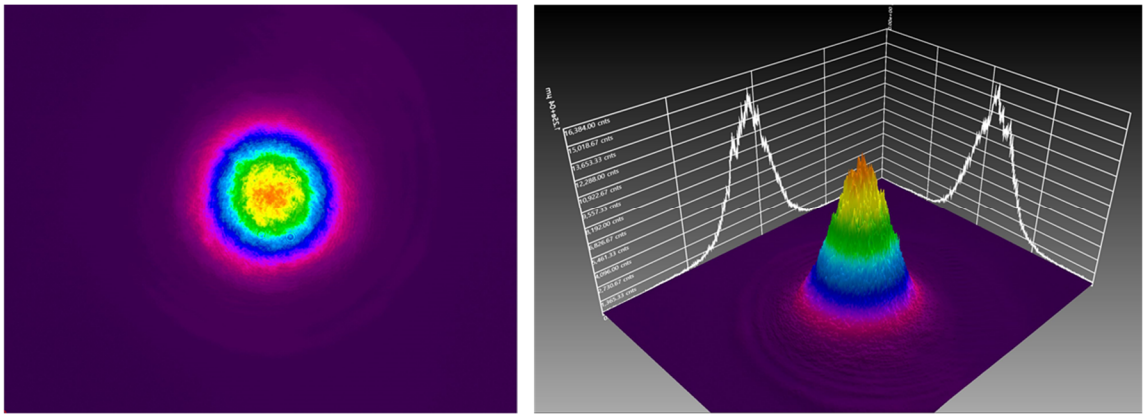

Supplementary Fig. 21 | Profile of Gaussian beam utilized in the laser lift-off processes.

Parameter	Value	Reference
Density of PI [$g \cdot cm^{-3}$]	1.42	[26]
Density of graphene [$g \cdot cm^{-3}$]	2.21	[38]
Density of glass [$g \cdot cm^{-3}$]	2.37	[39]
Specific heat of PI [$J \cdot g^{-1} \cdot K^{-1}$]	$2.55 - 1.59 \times \exp[(T_0 - T)/460]$	[26]
Specific heat of graphene [$J \cdot g^{-1} \cdot K^{-1}$]	0.709	[38]
Specific heat of glass [$J \cdot g^{-1} \cdot K^{-1}$]	$1.53 - 0.79 \times \exp[(T_0 - T)/638]$	[39]
Thermal conductivity of PI [$W \cdot cm^{-1} \cdot K^{-1}$]	$1.55 \times 10^{-3} (T/T_0)^{0.28}$	[26]
Thermal conductivity of graphene [$W \cdot cm^{-1} \cdot K^{-1}$]	$26.4 \times (T/T_0)^{-1.38}$	[40]
Thermal conductivity of glass [$W \cdot cm^{-1} \cdot K^{-1}$]	$7.9 \times 10^{-4} T^{0.43}$	[39]
Absorption coefficient of PI [cm^{-1}]	0.2×10^5	[41]
Absorption coefficient of graphene [cm^{-1}]	$\ln(10) \times 0.035 / (t_{Gr} \times 10^{-7})$	-
Absorption coefficient of glass [cm^{-1}]	2.107	Product datasheet provided by Corning

Supplementary Table 1 | Material properties assigned in the simulation.

Supplementary references

S1. Kappes, R. S. et al. A study of photothermal laser ablation of various polymers on microsecond time scales, *SpringerPlus* **3**, 489 (2014).

S2. Rahman, M. A. et al. Design of tough adhesive from commodity thermoplastics through dynamic crosslinking, *Sci. Adv.* **7**, eabk2451 (2021).